Available online at www.sciencedirect.com
ScienceDirect
ELSEVIER
C. R. Physique 9 (2008) 169–183
COMPTES RENDUS
PHYSIQUE
http://france.elsevier.com/direct/COMREN/

Recent developments in terahertz optoelectronics/Développements récents en optoélectronique térahertz

Laser terahertz emission microscopy

Hironaru Murakami, Masayoshi Tonouchi *

Institute of Laser Engineering, Osaka University, 2-6 Yamadaoka, Suita, Osaka, 565-0871, Japan

Available online 9 January 2008

Abstract

Laser terahertz (THz) emission microscopy (LTEM) is reviewed. Femtosecond lasers can excite THz waves in various electronic materials due to ultrafast current modulation. The current modulation is realized by the acceleration or deceleration of photo-excited carriers, and thus LTEM visualizes the dynamic photo-response of substances. We construct a free-space type and scanning probe type with transmission or reflection modes. The developed systems have a minimum spatial resolution better than 2 μm, which is defined by the laser beam diameter. We present some examples of LTEM applications, such as ferroelectric domain imaging, quantitative supercurrent distribution in high-T_c superconductors, defect detection of MOS devices as well as the visualization of the photo-responses in materials and devices. ***To cite this article: H. Murakami, M. Tonouchi, C. R. Physique 9 (2008).***
© 2007 Académie des sciences. Published by Elsevier Masson SAS. All rights reserved.

Résumé

Microscopie à émission térahertz photodéclenchée. Nous présentons une revue des recherches concernant la microscopie à émission térahertz photo-déclenchée. Des impulsions lasers de durée femtoseconde peuvent générer des ondes THz dans la plupart des semi-conducteurs de l'électronique, par l'intermédiaire du courant impulsionnel photogénéré. Ce courant est produit par l'accélération des photo-porteurs, et la microscopie à émission THz permet une visualisation résolue en temps de ce courant, donc du champ électrique à la surface des échantillons. Nous avons construit des sondes permettant un balayage spatial travaillant en mode de réflexion ou de transmission. Les systèmes réalisés montrent une résolution spatiale minimum meilleure que 2 μm, qui est définie par la taille du spot laser. Nous présentons quelques exemples d'application de ce microscope telle que l'imagerie de domaines ferroélectriques, la distribution quantitative du super-courant dans les supraconducteurs à haut T_c, la détection de défauts dans des structures CMOS et la visualisation de la réponse de matériaux et dispositifs. ***Pour citer cet article : H. Murakami, M. Tonouchi, C. R. Physique 9 (2008).***
© 2007 Académie des sciences. Published by Elsevier Masson SAS. All rights reserved.

Keywords: Terahertz emission; Scanning laser imaging; BiFeO; Superconductors; LSI

Mots-clés : Émission térahertz ; Imagerie laser à balayage ; BiFeO ; Supraconducteurs ; LSI

1. Introduction

Recent progress of terahertz (THz) technology is now bringing forth new research fields in both science and applications [1]. A variety of electronic materials can emit THz radiation upon being illuminated with femtosecond laser

* Corresponding author.
E-mail address: tonouchi@ile.osaka-u.ac.jp (M. Tonouchi).

1631-0705/$ – see front matter © 2007 Académie des sciences. Published by Elsevier Masson SAS. All rights reserved.
doi:10.1016/j.crhy.2007.07.010

[2–5]. The emission properties such as amplitude and waveforms reflect the nature of materials. Thus THz emission spectroscopy, as well as THz time domain spectroscopy (THz-TDS), have become important for exploring material science [6–22]. When one excites the THz emission from a certain substance and constructs the emission image by scanning the laser beam on it, the system works as a laser-THz emission microscope (LTEM) [23–33]. Since the resolution of the image is limited by the laser beam diameter rather than THz wavelength, sub-micron resolution images would be easily obtainable.

In this article, we review the development of LTEM and give some examples of applications.

2. THz wave emission by femtosecond laser pulse

THz wave emission excited by a femtosecond laser pulse occurs due to ultrafast current modulation, according to the classical formula of electrodynamics, $\boldsymbol{E} \propto \mathrm{d}\boldsymbol{J}/\mathrm{d}t$, where $\boldsymbol{E}$ is a radiated electric field in the far-field approximation and $\boldsymbol{J}$ is current.

Fig. 1 shows an example of THz radiation waveform emitted from a high-T_c superconductor (HTS) thin film. The THz wave emission phenomenon in HTS materials is a very unique one, compared with those for the other substances [17], such as semiconductors, ferroelectric materials, etc. The optical pulse produces a great number of quasiparticles by avalanche effects, followed by direct excitation of Cooper pairs, because the magnitude of superconducting gap ($\sim$10 meV) is considerably smaller than the photon energy (typically $\sim$1.5 eV in our case). Then, the excited quasiparticles relax to the superconducting condensed state within several picoseconds. Therefore, the introduction of a femtosecond laser pulse into HTS materials, with an applied bias current, causes an ultrafast supercurrent reduction at the limited regions corresponding to the illumination spot. Since the total number of excited quasiparticles by avalanche effects is approximately proportional to the supercarrier density at the illuminated regions in addition to the injection number of photons, the THz wave pulse with an amplitude which is almost proportional to the local supercurrent density is emitted. (See Fig. 15.)

On the other hand, the THz radiation from other semi-insulating materials, such as semiconductors, ferroelectric materials, etc., is generally caused by ultrafast modulation of optically induced current. In these cases, the introduction of a femtosecond laser pulse directly generates photo-excited carriers, and the THz wave pulse, with an amplitude proportional to the local electric field, is emitted,

Therefore, we can evaluate the magnitudes of the local supercurrent density and the local electric field in HTS materials and the other semi-insulating materials, respectively, by detecting the amplitudes of the THz wave pulses. Furthermore, since the sign of the THz wave pulse depends on the directions of the supercurrent or electric field, we can image the vector mapping of these electric elements in the samples with a spatial resolution of laser beam diameter by scanning the femtosecond laser beams [26].

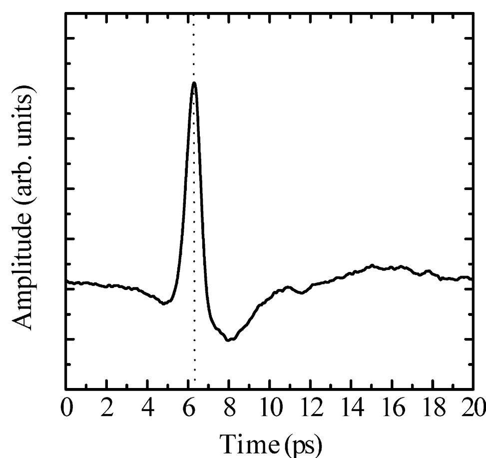

Fig. 1. Time domain waveform of THz wave pulse emitted from $YBa_2Cu_3O_{7-\delta}$(YBCO) thin film.

3. LTEM systems

3.1. Basic LTEM system

The optical diagram of the basic LTEM system is schematically illustrated in Fig. 2. Femtosecond optical pulses with a pulse-width of 80–100 fs are used as the optical source. The pump pulses, split from the trigger pulses, are delivered in free space alignment, and focused onto the sample mounted on a computer controlled x–y stage by using focusing optics. The generated THz waves are collimated and focused by a pair of parabolic mirrors onto the detector through a silicon hemispherical lens. Typically, we use a bow-tie antenna type photoconductive switch made of a low-temperature grown GaAs as a detector.

To obtain the THz images, we can use the THz waves reflected from or transmitted through the sample. The composition of a transmission system in which the input and detection optics can be independently constructed at the opposite sides of the sample with a high spatial resolution, is possible, but it can be applied only to thin film samples or the thick samples which are almost transparent for the THz waves, because the generated THz waves may be extremely attenuated in the samples.

On the other hand, the reflection type system is more useful for applications, because it can be applied to a variety of samples and composed as a compact system. However, the compact system is generally more complicated than that of the transmission type, because we have to compose both the input and detection optics on the same side of the sample. For the prototype reflection system as shown in Fig. 2, we composed the system by using a special parabolic mirror with a hole of $\phi = 3$ mm-diameter at the center, which enables us to introduce the pump beam pulses to a sample surface and to collect the THz waves generated at the irradiation spot in the front side of the sample.

The acquisition time of the THz image is one of the important factors for several applications. It depends on the total number of pixels in the LTEM image, and the time constant of a lock-in amplifier. The time constant was set at 1 or 3 ms. Therefore, it takes about 10–25 minutes for one frame scanning 500×500 pixels.

To demonstrate the performance of the basic LTEM system (reflection type), we selected a commercial operational amplifier (LM301AH, National Semiconductor) as a test sample [25]. For the measurements the metal can was removed, and the bare integrated circuits (IC) were directly illuminated by pump beams. LTEM images of the IC were obtained while driving the circuits as an inverting amplifier. The external connections with resisters are schematically illustrated in Fig. 3 (right).

Fig. 3(a) shows a LTEM image obtained at a condition of input voltage $V = 10$ V. The image is superimposed on the optical microscope image of the IC chip. The red and blue regions indicate positive and negative electric fields of THz waves emitted from the circuits, which also correspond to positive and negative electric fields in the x direction in the circuits, respectively. This THz emission image was measured while the pump beam was being modulated. Therefore, all the terahertz waves emitted from the local regions applied with some bias voltages in the circuits are observable.

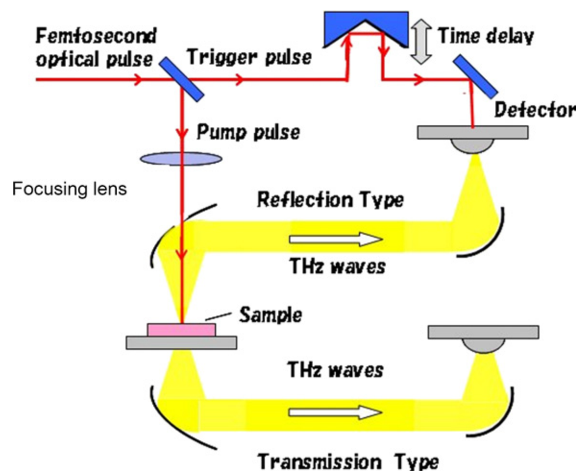

Fig. 2. Schematic illustration of the experimental setup for basic LTEM system.

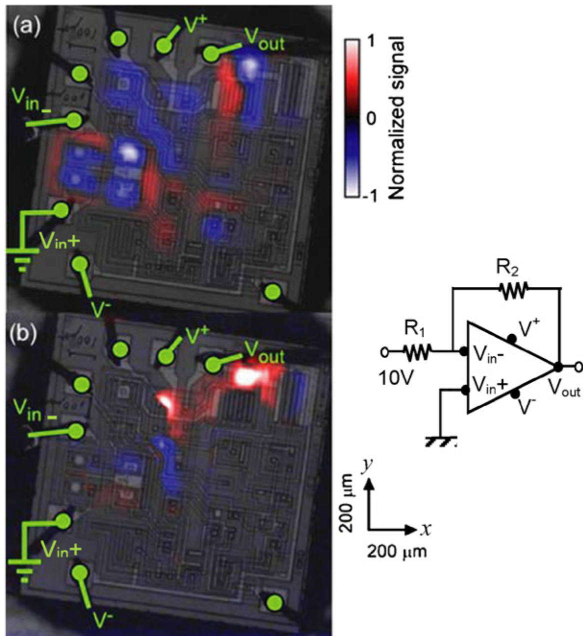

Fig. 3. LTEM images of the biased IC chip superimposed on optical images. Green dots indicate the terminals of the IC chip. The red and blue regions indicate an electric field with positive and negative directions along the x-axis, respectively. The color scales are normalized for the maximum value of the detected signal. The images were measured by modulating (a) the pump laser power and (b) the voltage signal applied to V_{in}.

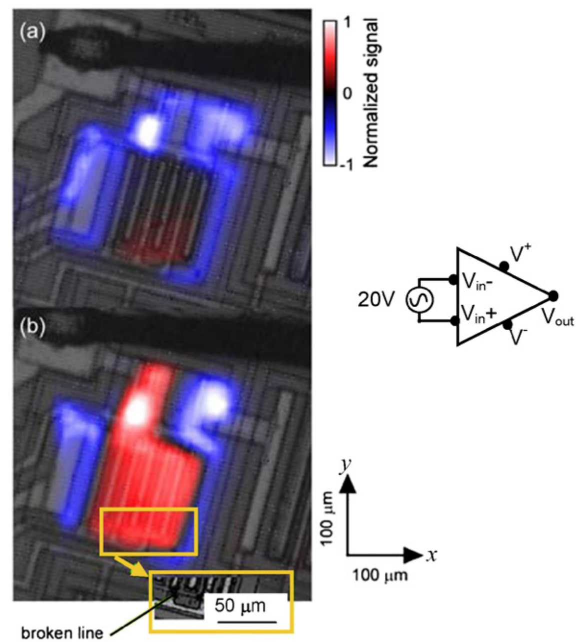

Fig. 4. LTEM images of (a) a normal and (b) a broken IC chip. The color scales are normalized using the maximum value. A modulated voltage signal was applied between two terminals. Insert shows a magnified photograph of the area containing the broken line.

On the other hand, Fig. 3(b) shows an image measured without applying the optical modulation, but applying a voltage modulation at 2 kHz to the input resister R_1. Synchronizing the input voltage with the lock-in amplifier enables us to detect limited THz waves emitted from the regions through which the modulated input signal passes. Here, it can be seen that the input signal is gradually amplified as it passes from the input terminal to the output terminal of the circuit. Therefore, we can easily retrace each signal line separately by changing the terminal to be electrically modulated.

To demonstrate practical fault inspection in ICs, we prepared a damaged sample by intentionally cutting a single interconnection line (see insert in Fig. 4(b)). LTEM images of the normal and broken chip are shown in Figs. 4(a) and (b), respectively. A modulated signal was applied between two input terminals with a peak-to-peak voltage of 20 V at 2 kHz, without any connection with the resisters (i.e. a comparator type circuit). As shown here, these two images are clearly different, particularly in the red region. These results indicate that the LTEM images of IC chips drastically change due to a fault in the circuit, and show the possibility that this technique is applicable to the identification of the failed circuit block in the IC chip.

Here, we demonstrated the results observed for an IC chip as one example that shows the utility of the reflection type LTEM system. It shows one possibility of this system to be utilized to specify the failed circuit block in an IC chip. However, since we have to use focusing optics with a long focal length, which brings a poor numerical aperture (NA) value, in the prototype system, the pump beam spot size of only ∼20 μm could be attained, which is insufficient to specify the detailed failed circuit block. Therefore, we developed further new versions of LTEM systems with higher resolution, as discussed below.

3.2. Advanced LTEM system

In this section, an advanced version of the LTEM system with a high spatial resolution is presented. To improve the spatial resolution of the prototype LTEM system of reflection version, we introduced an indium tin oxide (ITO)

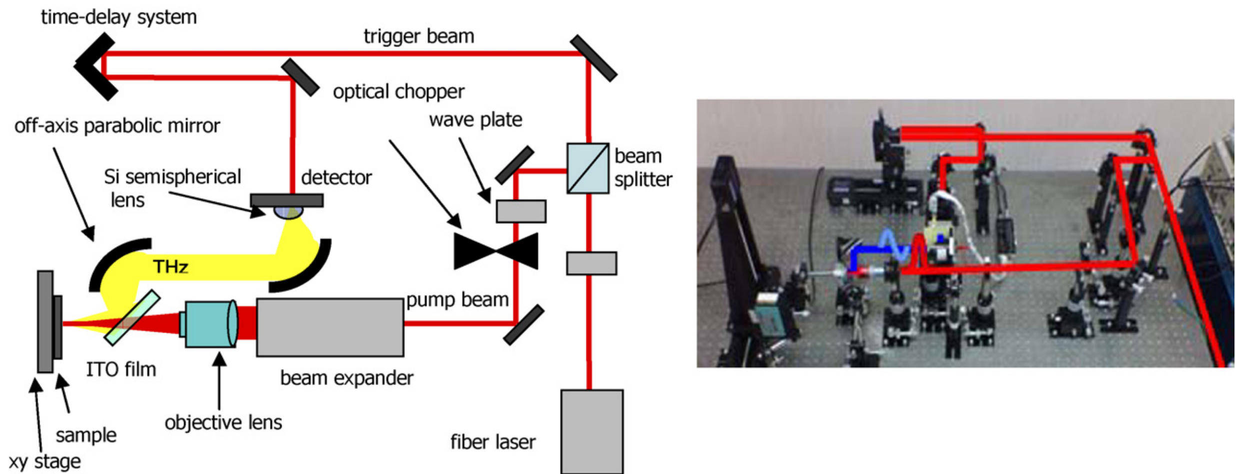

Fig. 5. Schematic illustration of the experimental setup for advanced reflection type LTEM system (left), and its picture (right).

thin film, grown on a glass plate substrate, into the system as a beam selector [27]. It is almost transparent for visible light and highly reflective for the THz waves. By introducing it between a sample and the focusing optics, we can reduce the distance between them, and increase the beam diameter at the front side of a sample. The relaxation of these limitations allows us to adopt suitable focusing optics with a high NA value.

Fig. 5 shows the optical diagram of the advanced system and a picture of it. A mode-locked femtosecond laser based on Er-doped fiber oscillator is used as an optical source (center wavelength: 780 mm, pulse width: 100 fs, repetition rate: 50 MHz). In this setup, to improve the spatial resolution, we introduced an objective lens with a high NA value as the focusing optics and a beam expander. The pump beams enter the objective lens after being expanded by a couple of convex lenses and illuminate the sample mounted on a computer controlled x–y stage. By expanding the incident beam diameter Φ, we can improve the beam spot size ϕ, according to the following relation,

$$\phi = \frac{4}{\pi}\lambda\frac{f}{\Phi}$$

where λ is the wavelength, and f the focal length of the objective lens. The emitted THz waves from the sample surface are reflected by the ITO thin film and effectively collimated and focused onto a LT-GaAs bow-tie antenna-type photoconductive switching detector by using a pair of off-axis parabolic mirrors and a Si semispherical lens. The detector is mounted on a holder so that the gap direction becomes horizontal, and the switch is gated by trigger beams which are split off from the pump beams and arrive at the detector after passing through the time-delay optics. Sample scanning for acquiring THz images is carried out by fixing the time-delay at the peak position in the time-domain waveform (for example, 6.3 ps in Fig. 1).

Since the spatial resolution of the LTEM image is strongly influenced by the spot size of the pump beams, we first checked the effect of the introduction of the beam expander by measuring the power profiles of the focused pump beam using a commercial beam profiler. Here, we composed the beam expander with a magnification of 3 times. Fig. 6 shows the results observed under several conditions. Fig. 6(a) shows a beam power profile of pump laser beam without any optics. It can be seen that the diameter of the pump laser emitted from the fiber laser is about 1.6 mm. On the other hand, Figs. 6(b) and (c) show the power profiles of the pump beam after passing through an objective lens (Mitsutoyo M PLAN APO 20, NA = 0.4) with and without the beam expander. Comparing these results, the introduction of the beam expander has an certain effect on reducing the beam spot size down to about 73% (2.2 μm diameter). Furthermore, since the beam spot size in the prototype LTEM system was at most about 20 μm, it is obviously expected that the introduction of the objective lens is effective in improving the spatial resolution.

To evaluate the spatial resolution of the advanced LTEM system, we measured test samples consisting of several gold line and space patterns fabricated on a Fe-doped semi-insulating InP substrate. Figs. 7(a) and (b) show the optical microscope images of the test patterns. The width of the lines and spaces are same in each pattern: (a) 2.0 μm and (b) 1.5 μm. Fig. 8(a) shows a THz wave emission image (upper) and line scan profile (lower) observed at a zero bias voltage condition without the beam expander. In the zero bias voltage condition, only the photo-excited carriers at

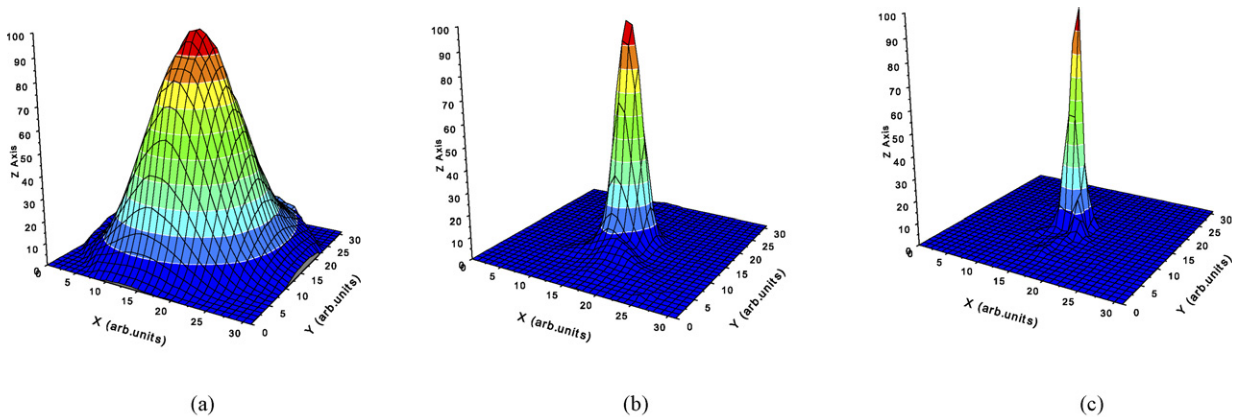

Fig. 6. Pump beam power profiles observed under several conditions: (a) emitted from the fiber laser; (b) after passing through an objective lens; and (c) after passing through the objective lens and beam expander with a magnification of 3.

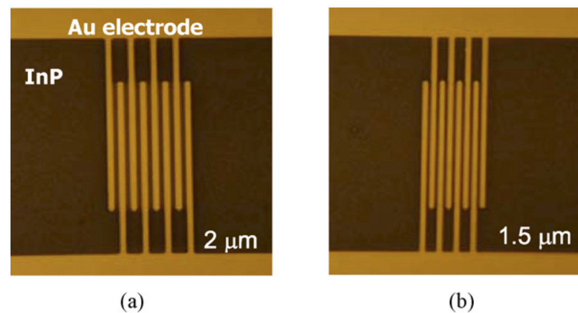

Fig. 7. Gold line and space patterns on Fe-doped semi-insulating InP. The widths of the line and space are same: (a) 2 μm; and (b) 1.5 μm.

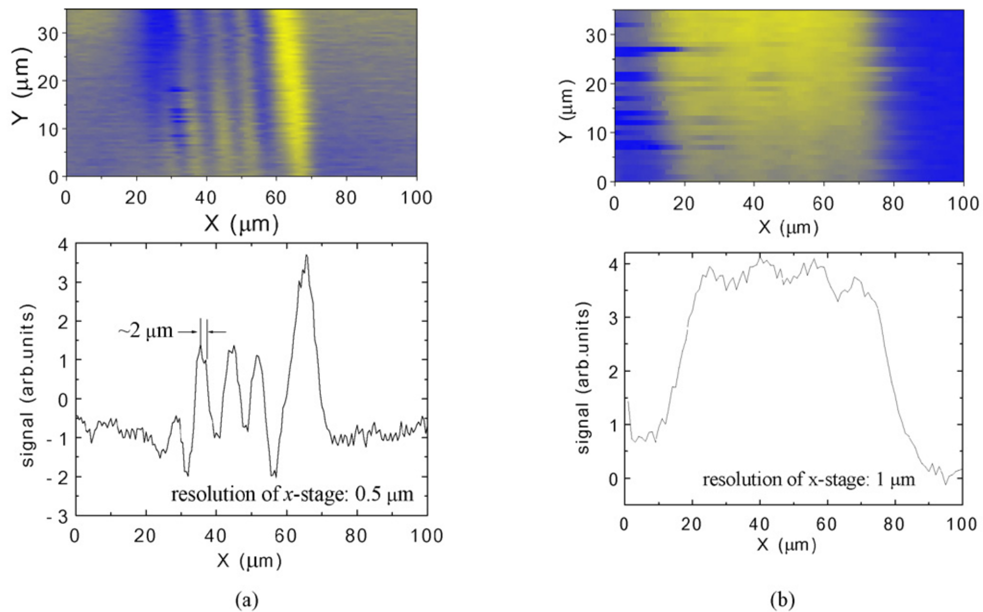

Fig. 8. (a) A LTEM image (upper) and a line scan profile (lower) observed on the 2 μm-line and space pattern at zero bias voltage condition. The observations were carried out without the introduction of a beam expander. The resolution of the x–y stages is 0.5 μm. (b) A LTEM image (upper) and a line scan profile (lower) observed on the 2 μm-line and space pattern applied with a DC bias voltage of 1 V. The observations were carried out without introduction of a beam expander. The resolution of the x–y stages is 1.0 μm.

the boundary regions between the gold electrodes and InP substrate can produce the transient photocurrents being accelerated by the built-in electric field, and injected into the gold electrode. Since the injected hot carriers have high energies compared to those of free carriers in gold, they can also produce transient currents until they lose the extra energy by scattering. Therefore, the electromagnetic waves with the electric field elements along the gold line (vertical elements) will be also emitted into the free space, beside the horizontal elements across the boundaries. Thus, it will strongly depend on an interfacial energy profile, and on the thickness of the depletion layer, etc., where the signal is stronger.

As for the THz wave image in Fig. 8(a), yellow and blue lines are alternately visible, reflecting the periodical structure of the line and space patterns. Moreover, it can be seen that these lines are slightly inclined. If the gap direction of the bow-tie antenna switch was correctly perpendicular to the line and space directions, we cannot observe the vertical elements of THz waves along the gold lines. However, the existence of some inclination of the line and space, as shown in the THz image, enables us to observe such electromagnetic wave elements, as well. From the analysis of the data obtained, in comparison with the real arrangements of the gold electrodes on the InP substrate, THz waves with the vertical elements are dominantly observed in this experiment. To confirm it, we applied a dc bias voltage of 1 V between the upper and lower gold electrodes and observed the THz wave emission image. Fig. 8(b) shows the observed THz wave emission image (upper) and line scan profile (lower). It can be seen from the line scan profile that only positive signals were observed in this experiment. If some intense THz waves with horizontal elements are generated between the parallel gold electrodes to which the dc bias voltage is applied, the sign of the signals change alternately from the space to space in the line–space pattern. These obtained results certainly indicate that the observed THz wave signals are mainly vertical elements along the gold lines.

On the other hand, two fine peak structures (with the intervals of about 2 μm) can be clearly seen on the positive and negative peaks in the line scan profile of Fig. 8(a), the positions of which almost correspond to those of the gold electrodes. If we limit the discussion to the vertical elements along the gold lines, the intensities of THz wave signals generated at both the boundary sites of a gold electrode become almost same, because the energy profiles at both the interfaces with the InP substrate are symmetrical with respect to the gold electrode. On the other hand, if the pump beams illuminate the center of a gold electrode, the signal intensities become weak. Therefore, these two fine peak structures originate in the THz waves emitted from the boundary sites, and it indicate that the advanced system has a spatial resolution of at least ∼2 μm without the beam expander.

As for the effects of the introduction of the beam expander, Figs. 9(a) and (b) show the THz wave emission image and the line scan profile observed on the 1.5 μm-line and space sample, respectively. Although such fine structure as

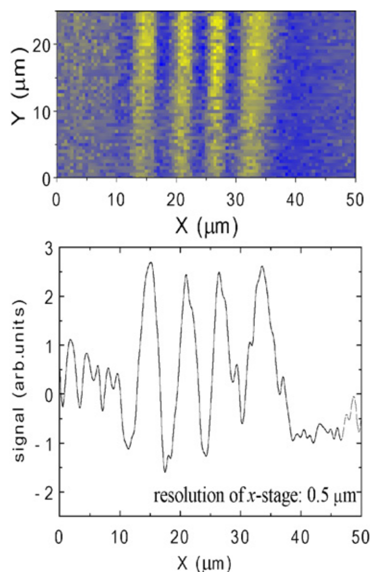

Fig. 9. (a) A LTEM image and (b) a line scan profile observed on the 1.5 μm-line and space pattern at a zero bias voltage condition. The observations were carried out with the introduction of the beam expander. The resolution of the x–y stages is 0.5 μm.

shown for 2 µm-sample is not observed on all the peak structures due to the poor resolution, 0.5 µm, of the present x–y stage, we have succeeded in the observation of almost the same line scan profile as that for the 2 µm-sample.

3.3. Scanning probe type LTEM

In this section, the development of a scanning probe LTEM (SP-LTEM) system is introduced. Using this system, we can exactly determine the position of the photo-excitation area in a sample by monitoring the sample surface, because the pump beam is irradiated through an optical-fiber probe in the vicinity of the sample surface. The large NA value of the probe lens inherently provides the tight focusing condition of the pump beam. Furthermore, the optical fiber probe greatly improves the operability of the system, and shows flexibility in terms of integration with a scanning near-field optical microscopy (SNOM) system as a future possibility.

Fig. 10(a) shows the optical diagram of the SP-LTEM system. A Ti:sapphire laser is used as an optical source (center wavelength: 780 nm, pulse width: 100 fs, repetition rate: 80 MHz). The beam is divided into the pump and trigger beams, and these beams are introduced into 4 m-single-mode optical fibers. The positive group-delay dispersion in the optical fibers is compensated by two compensators that consist of gratings and prisms for retroreflection. The sample surface is irradiated by the beam of the pump pulse through a commercial optical fiber probe. The optical-fiber probe is set above the sample surface at a distance of ∼5 µm by monitoring the sample surface with an optical microscope. The maximum power of the pump beam which is mainly determined by the coupling efficiency with the optical fiber (10–20%) is about 10 mW. On the other hand, the beam diameter is the most important factor to determine the spatial resolution. As for the beam diameter, we can apply the beam with the diameter as small as about 1.2 µm (commercial value) by selecting an appropriate optical fiber (e.g., some products supplied from Cascade Microtech, Inc.).

The THz waves emitted from the sample surface are collimated by an off-axis parabolic mirror (diameter, 25 mm; effective focal length, 50 mm) and focused onto the detector by a silicon hyper-hemispherical lens (radius, 6.75 mm; center offset, 3.5 mm). For the detector, we use a bow-tie type photoconductive switch antenna fabricated on a LT-GaAs substrate. The trigger beam is optically delayed and irradiated to the gap of the photoconductive switch with an average power of several mW. The amplitudes of the THz wave pulses are measured as a function of time using a lock-in amplifier, applying an optical/bias modulation of 2 kHz. The optical-fiber probe and detector are mounted on an automatic stage which keeps the sample at a fixed position. A photo of this system is shown in Fig. 10(b).

As for the effect of group-delay dispersion in the optical fibers on the THz emission, Fig. 11(a) shows the pulse width as a function of the amount of compensation for various transmitted powers through the optical fibers. Here, we obtained the bare pulse width Δt from the correlated pulse-width $\Delta t'$, which is measured by means of an autocorrelator, as $\Delta t = \Delta t'/\sqrt{2}$ assuming that the envelope waveform of the optical pulse is Gaussian. For a transmitted power

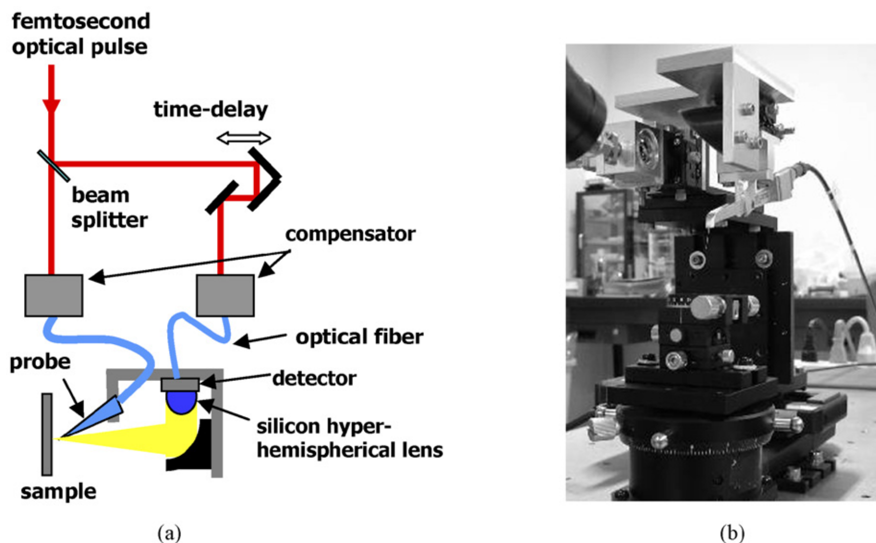

Fig. 10. (a) Optical diagram and (b) image of the SP-LTEM system.

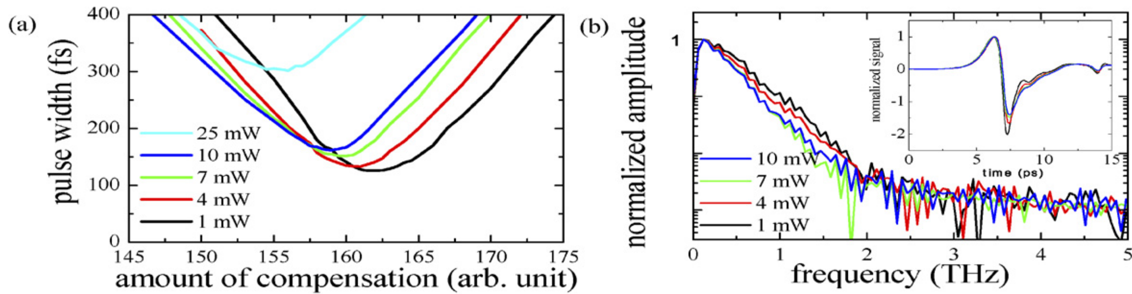

Fig. 11. (a) Effects of dispersion compensation in optical fibers on optical pulse widths. (b) THz normalized Fourier spectra for various optical excitation powers. The insert shows the corresponding time-domain waveforms.

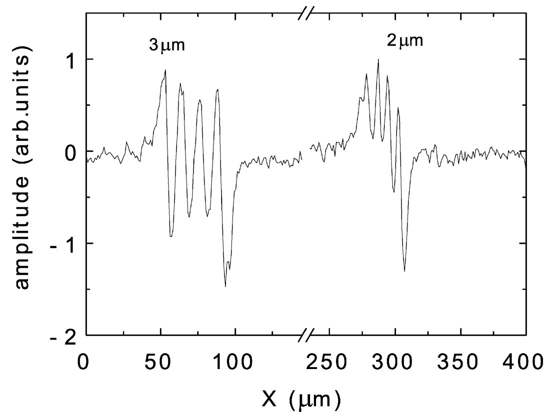

Fig. 12. Line scan profiles observed on the 3 μm-line and space pattern (left) and 2 μm-line and space pattern (right) at zero bias voltage condition.

of less than 10 mW, we can suppress the pulse width down to ∼150 fs after the transmission through the 4-m optical fibers. Due to higher-order dispersion in the optical fibers, that cannot be compensated by gratings, the minimum pulse width of ∼150 fs is still broader than the original pulse width of 100 fs. If the transmitted power exceeds 10 mW, nonlinear pulse broadening becomes prominent.

Next, we obtained the THz emission spectra varying the pump beam power, keeping the trigger beam power constant at 5 mW. The amount of compensation of the positive group delay dispersion in the optical fibers was always optimized, and dipole photoconductive switch antennas fabricated on LT-GaAs substrates were used for THz emission and THz detection. Fig. 11(b) shows the Fourier spectra of emitted THz wave pulses, together with the corresponding time-domain waveforms in the insert. For a pump pulse power of less than 10 mW, the peak amplitude of the emitted THz waves is almost proportional to the pump pulse power. Even for low transmitted powers, however, we can recognize slight changes in the time-domain waveforms and THz emission spectra, which are thought to be due to the nonlinear broadening of the pump pulse.

To evaluate the spatial resolution of the SP-LTEM system, we prepared gold line and space patterns on a LT-GaAs substrate. For a given sample, the width of the line and space is same: 3 or 2 μm. Fig. 12 shows the line scan profiles observed with an optical fiber probe (beam spot size: 5 μmϕ@commercial value) under zero bias voltage condition. An almost similar signal pattern to that in Fig. 8(a) is shown for the 3 μm-line and space sample, while a more asymmetrical pattern is shown for the 2 μm case. From these results, it is deduced that the fabricated SP-LTEM system has a spatial resolution of ∼3 μm, which is a little better than that expected from the beam spot size as a commercial value.

As shown above, using the optical fiber probe, we can realize a compact LTEM system without loss of spatial resolution.

4. Applications

4.1. Visualizing ferroelectric domains

The THz waves are generated by means of optical carrier excitation followed by either its acceleration or deceleration due to transient polarization. In general, the emission properties are governed by the nature of the material, such as carrier mobility, mechanism of conductivity and/or photoexcitation, local built-in electric field, and ferroelectricity, as well as an external contribution such as the bias field. Thus LTEM could be a strong research tool for material science. As one such application, we show an example of ferroelectric domain imaging.

Typical ferroelectric materials have a large optical band gap in the ultra-violet region, which makes it difficult to generate THz waves via optical carrier excitation using a Ti:sapphire laser at around a wavelength of 780 nm. Here we select as a sample $BiFeO_3$, which has a relatively small energy gap of about 2.5 eV. $BiFeO_3$ is a multiferroic material displaying ferroelectricity below 1100 K and antiferromagnetism below 640 K, which, in addition, exhibits an extremely large spontaneous polarization P_s in thin film form, providing its potential as a capacitor in various electronic devices. Accordingly, studies on $BiFeO_3$ have mainly been focused on developing its electronic functionality as a capacitor, and its optical functionality, on the other hand, has not been investigated intensively so far.

The second harmonic of a mode-locked Ti:Sapphire laser is used for carrier excitation, giving rise to THz radiation. 200 nm-thick $BiFeO_3$ thin films are grown on $(LaAlO_3)_{0.3}(Sr_2AlTaO_6)_{0.7}(001)$ substrates by the pulsed laser deposition technique with a KrF excimer laser. A dipole-type photoconductive switch with a pair of Au electrodes is designed on the film by a conventional lift-off process and sputtering method. The Au electrode of the photoconductive switch consists of a pair of 30 µm-wide strip lines separated by 20 µm with a dipole gap of 10 µm. Details of the experiments can be found elsewhere [30,31].

Fig. 13(a) shows two time-domain THz waveforms radiated from the $BiFeO_3$ photoconductive switch measured at zero-bias electric field, after applying a bias electric field E_{bias} of ± 200 kV/cm. The THz waveforms show an identical Fourier transformed amplitude spectrum exhibiting a frequency component extending up to 1 THz (Fig. 13(b)) and obviously, have a phase reversed by π with one another. This feature definitely expresses a ferroelectric peculiarity that the history of E_{bias} is memorized and the remnant polarization of $BiFeO_3$ substitutes for E_{bias}. Further supporting this aspect, a distinct feature was observed as we measured the main peak amplitude of the THz pulse E_{THz} as a function of E_{bias} (Fig. 13(c)). In the photoconductive switches reported so far, which are all non-ferroelectric materials, E_{THz} generally has a linear relationship with the applied E_{bias} reversing its phase by π when the polarity of E_{bias} is reversed. However, in the case of $BiFeO_3$, we observed a clear hysteresis loop which looks similar to the typical polarization hysteresis loop observed in common ferroelectrics. These characteristics strongly indicate the direct relationship of THz radiation with Ps, and imply that the THz radiation here is derived from the ultrafast Ps modulation introduced by the mobile photoexcited charge carriers.

Since the THz radiation is exhibiting a direct relationship with the polarization state, using LTEM to measure E_{THz} allows us to visualize the ferroelectric domain structures by distinguishing the polarization states from the signs of E_{THz}. In Fig. 14, two kinds of ferroelectric domain images of a section of the $BiFeO_3$ thin film measured at zero-bias voltage after applying a bias voltage V_{bias} of ± 200 V are shown. Domains with opposite polarization states appear as blue and red areas depending on the sign of E_{THz}. By comparing the two images, one can see that only the domains between the electrodes have changed their states by the application of the opposite V_{bias}, while the other areas are independent of V_{bias} and remain unchanged. Note that we also observed THz radiation even in areas away from the electrodes where the domains have not been artificially aligned. However, the intensity of E_{THz} in these areas is relatively weak, presumably because the domains are not so aligned as it is the case between the electrodes. These imaging results indicate that THz radiation occurs from individual ferroelectric domains and the intensity of E_{THz} is determined by the average of the electric dipole moments which the laser spot covers.

4.2. Quantitative evaluation of supercurrent distribution

Quantitative evaluation of material parameters by LTEM would open wider research applications. Fig. 15 shows the THz emission amplitude as a function of supercurrent in YBCO thin films. The amplitude increases in proportion to the bias-current regardless of the laser power except near a phase transition. Thus one can quantitatively evaluate

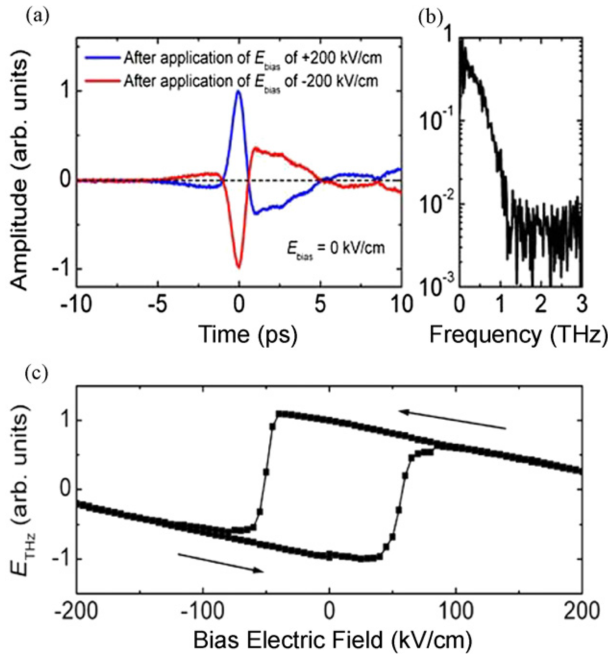

Fig. 13. Terahertz (THz) radiation characteristics of $BiFeO_3$ thin films. (a) Time-domain waveforms of the THz pulse radiated from a $BiFeO_3$ film. The measurement was performed at zero-bias electric field after applying a bias electric field E_{bias} of ±200 kV/cm. The dashed line represents the zero-level line shown for clarity. (b) Fourier transformed amplitude spectrum of the time-domain waveforms shown in (a). Both waveforms exhibit the same power spectrum since the two waveforms show a similar shape, differing only with their phase shifted by π. (c) The amplitude of the radiated THz pulse E_{THz} as a function of E_{bias}. The arrows indicate the sequential direction, starting by applying E_{bias} of +200 kV/cm.

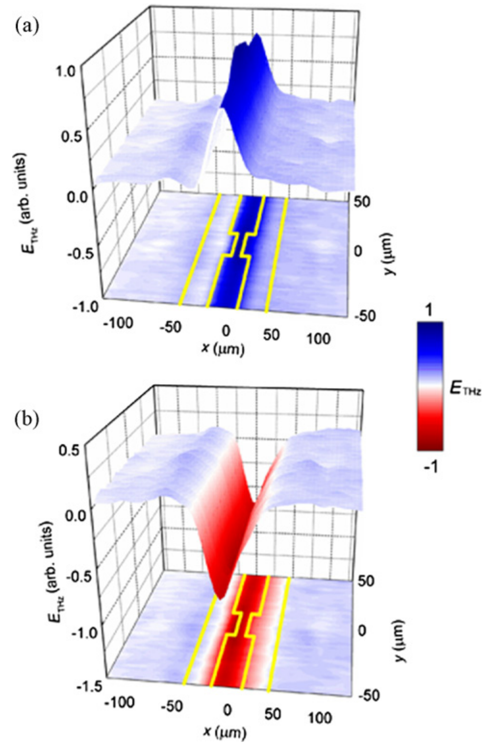

Fig. 14. Visualization of 180° ferroelectric domain structure of a $BiFeO_3$ thin film, probing with terahertz (THz) radiation. Domain structure under zero-bias voltage measured after applying (a) +200 V and (b) −200 V. The geometry of the dipole-type gold electrodes is also shown by the yellow line in the two images. The spatial resolution here is thought to be about 20 μm, estimated from the diameter of the laser spot.

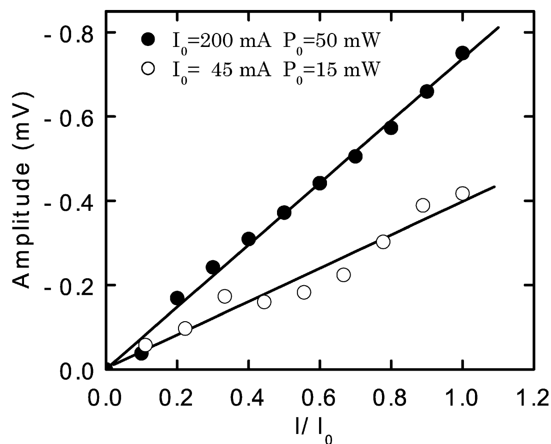

Fig. 15. THz emission amplitudes, as a function of normalized supercurrent I/I_0 in YBCO thin films.

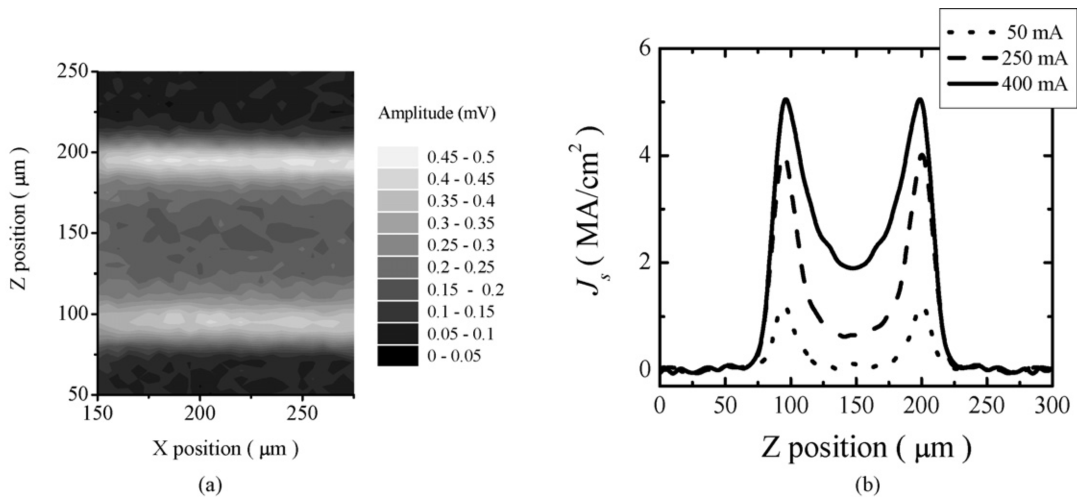

Fig. 16. (a) THz wave image of supercurrent distribution in YBCO strip line. (b) Supercurrent distributions along z direction calculated using a calibration technique in Ref. [32].

supercurrent distributions in superconductors after calibrating the relationship between the amplitude and transport current.

To visualize the distribution, a movable sample holder is connected to cold base of the refrigerator. The delay time was fixed at the maximum amplitude position in the THz radiation waveform, and then the laser beam was scanned by translating the sample. The spatial resolution was limited by the laser spot size; 25 µm in this case. A bow-tie-antenna-type LT-GaAs photodetector is used to detect the THz waves. 100 nm thick YBCO thin films are patterned into 114 µm-wide strips using conventional photolithographic techniques and Ar ion milling. After the sample is cooled down to 17 K without an intentional external field, the supercurrent distributions are examined. A laser power of 5 mW for the THz radiation imaging is used, so that no significant distortion is induced due to laser exposure. The detail for the experimental condition and data processing procedure has been reported elsewhere [32].

Fig. 16(a) shows an example of the two-dimensional image of the THz radiation amplitude. We see that the supercurrent distribution is clearly visualized by LTEM. The amplitude distributions along the z direction are quantitatively transferred into the supercurrent density distributions, for various bias currents as plotted in Fig. 16(b), using a calibration technique as reported in Ref. [32]. Furthermore, one can even quantitatively evaluate the magnetic field induced by either the transport current or trapped vortices (see Ref. [33]).

4.3. Defect localization in semiconductor devices

The inspection and failure analysis of semiconductor devices has become a critical issue with increasing demands for quality and reliability in circuits [34–36]. Currently LSI failure analysis uses emission microscopy, infrared optical-beam-induced resistance-change and electron beam testing to the localize electrical failure position nondestructively. These methods unfavorably require an electrical contact with the LSI chip, generally. Recently, we have developed a laser-THz emission microscope (LTEM) that offers the possibility of noncontact and nondestructive inspection of the electrical failures in circuits [25,27–29]. Here we show experiment results observed on a LSI-8 bit microprocessor and on unbiased MOSFETs embedded in a test element group (TEG) measured by LTEM.

We measured an LSI 8-bit microprocessor [27] (custom chip based on the MPU 6502 model supplied by MOS Technologies, Inc.), which has 3 µm-wide interconnection lines. The measurements were carried out under a bias voltage condition of 3 V by applying optical modulation at 2 kHz. The LTEM image superimposed on an optical image is shown in Fig. 17. The red and blue regions indicate THz emissions with positive and negative amplitudes, respectively, which correspond to the directions of the electric field. To evaluate the resolution, right-bottom in Fig. 17 shows a magnified THz image of a small area in the microprocessor chip, rescanned at a pixel size of 1×1 µm^2. Here,

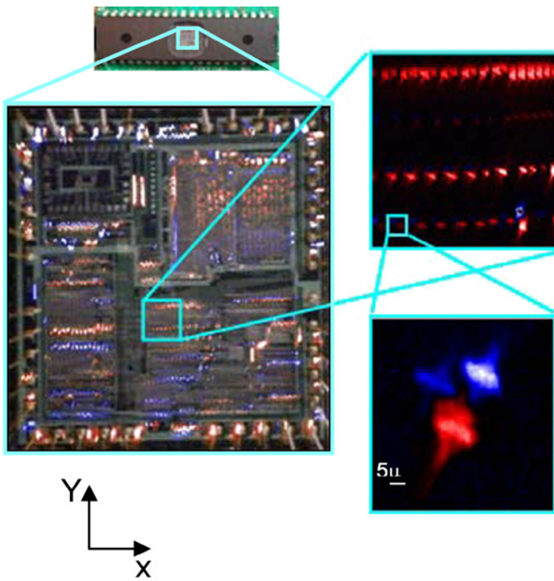

Fig. 17. LTEM images observed on a LSI 8-bit microprocessor (custom chip based on the MPU 6502 model supplied by MOS Technologies, Inc.).

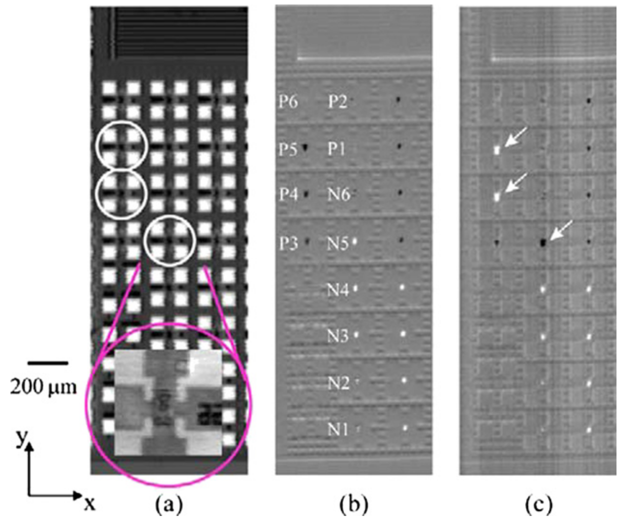

Fig. 18. (a) LTEM image of a series of MOSFETs; (b) the normal sample; and (c) the damaged sample. The damaged sample has three MOSFETs having interrupted connection lines, as indicated by the white circles in Fig. 18(a).

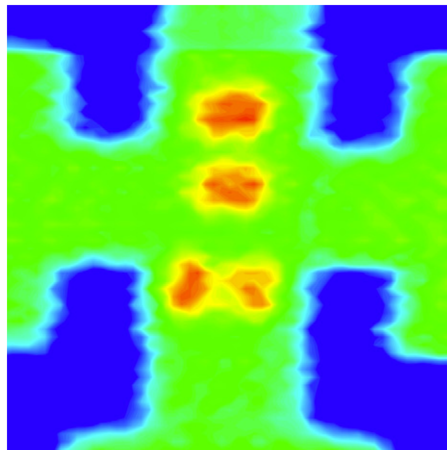

Fig. 19. Reflection LTEM image of the region in the center of the magnified image in Fig. 18(a): red areas are p–n junctions; blue ones are electrode pads.

the detailed THz emission patterns comparable to the 3 μm-wide interconnection line can be seen, and this result shows that the spatial resolution has been considerably improved compared with that of a basic LTEM system.

On the other hand, MOSFETs fabricated in a TEG prepared for the evaluation of the semiconductor devices are examined [28]. Fig. 18 shows the laser-reflection image (a) and the LTEM images ((b) and (c)) of MOSFETs measured under zero bias condition. In Fig. 18(a), the white squares are the electrodes of the twenty MOSFETs in this image. The contrast in the THz emission image in Fig. 18(b) is due to the built-in electric fields that are induced by the energy band bending at the various interfaces, such as p–n junctions and Schottky contacts.

The LTEM image from a damaged TEG sample is shown in Fig. 18(c). The bright and dark gray levels correspond to the positive and negative amplitude of the THz emission, respectively. The connection lines of the three MOSFETs circled in Fig. 18(a) were interrupted by using a focused ion beam to simulate damaged MOSFETs. One can see that the sign of the THz emission amplitude from p–n junctions in damaged MOSFETs, indicated by white arrows in

Fig. 18(c), changes in comparison with that of normal MOSFETs, which means that the polarity of the THz waveform has reversed. Although at present this mechanism is still unclear, the results indicate that LTEM is the potential tool for LSI defect analysis.

The front surface of the LSI is covered by a number of metal wires and contacts which hinder the THz excitation. In order to apply LTEM for the LSI failure analysis, fs pulses should be lead from the backside and the reflected THz waves should be detected. Since the optical pulses at a wavelength of around 780 nm are absorbed by the Si wafer, we have to select the wavelength of the laser so that the photons can arrive near the front surface and excite carriers in p–n junctions. Thus a pump laser with a wavelength of 1.05 μm is utilized for the backside illumination of silicon-based LSI chips [29]. THz amplitude in the region indicated by the red circle in Fig. 19, is measured from the substrate side under zero bias condition. Red contrast indicates the THz emission from four p–n channels embedded around the center of the MOSFET. The result indicates that successful LTEM imaging of Si MOSFETs can be obtained from the reflection type LTEM.

5. Summary and outlook

We have reviewed the principle and development of Laser Terahertz Emission Microscope (LTEM). The spatial resolution was greatly improved by optimizing the optical composition of the system, and, so far, 2 μm could be achieved as the spatial resolution. Several application examples demonstrated here show strongly that the LTEM has the potential not only in the electrical fault inspection in LSI circuits and the other diagnostic applications for various electronic devices, but also to explore material science for various materials.

Acknowledgements

This work was supported in part by the Strategic Information and Communications Research and Development Promotion Fund of Ministry of Internal Affairs and Communications (MIC), the Grant-in-Aid for Scientific Research (A) No. 16206036 from the Japan Society for the Promotion of Science (JSPS), and Special Coordination Fund for Promoting Science and Technology of the Ministry of Education, Sports, Culture, Science and Technology (MEXT).

Authors would like to express a great gratitude to Prof. T. Kiwa of Okayama University, Dr. M. Yamashita of RIKEN, Dr. K. Nikawa of NEC Electronics Corp., and Dr. R. Inoue, Dr. S. Kim, Mr. N. Uchida, and Mr. H. Koga from the Tonouchi Laboratory of Osaka University for their enthusiasm and efforts to accomplish these experiments.

References

[1] M. Tonouchi, Cutting-edge terahertz technology, Nature Photonics 1 (2007) 97–105.
[2] D.H. Auston, K.P. Cheung, P.R. Smith, Picosecond photoconducting Hertzian dipoles, Appl. Phys. Lett. 45 (1984) 284–286.
[3] Y. Jin, X.F. Ma, G.A. Wagoner, M. Alexander, X.C. Zhang, Anomalous optically rectification from metal/GaAs interfaces, Appl. Phys. Lett. 65 (1994) 682–684.
[4] X.C. Zhang, B.B. Hu, J.T. Darrow, D.H. Auston, Optically induced electromagnetic radiation from semiconductor surfaces, Appl. Phys. Lett. 56 (1990) 1011–1013.
[5] M. Tonouchi, M. Tani, Z. Wang, K. Sakai, N. Wada, M. Hangyo, Ultrashort electromagnetic pulse radiation from YBCO thin films excited by femtosecond optical pulse, Jpn. J. Appl. Phys. 35 (1996) 2624–2632.
[6] S.E. Ralph, D. Grischkowsky, Trap-enhanced electric fields in semi-insulators: The role of electrical and optical carrier injection, Appl. Phys. Lett. 59 (1991) 1972–1974.
[7] Y. Cai, I. Brener, J. Lopata, J. Wynn, L. Pfeiffer, J. Federici, Design and performance of singular electric field terahertz photoconducting antennas, Appl. Phys. Lett. 71 (1997) 2076–2078.
[8] B.B. Hu, M.C. Nuss, Imaging with terahertz waves, Opt. Lett. 20 (1995) 1716–1718.
[9] D.M. Mittleman, G. Gupta, B. Neelamani, R.G. Baraniuk, J.V. Rudd, M. Koch, Recent advantages in terahertz imaging, Appl. Phys. B 68 (1999) 1085–1094.
[10] D. Mittleman, R. Jacobsen, M.C. Nuss, T-ray imaging, IEEE J. Sel. Top. Quantum Electron. 2 (1996) 679.
[11] K. Kawase, Y. Ogawa, Y. Watanabe, Non-destructive terahertz imaging of illicit drugs using spectral fingerprints, Opt. Exp. 11 (2003) 2549–2554.
[12] Q. Chen, Z. Jiang, G.X. Xu, X.-C. Zhang, Near-field terahertz imaging with a dynamic aperture, Opt. Lett. 25 (2000) 1122–1124.
[13] O. Mitrofanov, M. Lee, J.W.P. Hsu, I. Brener, R. Harel, J.F. Federici, J.D. Wynn, L.N. Pfeiffer, K.W. West, Collection-mode near-field imaging with 0.5-THz pulses, IEEE J. Sel. Top. Quantum Elecron. 7 (2001) 600–607.
[14] H.-T. Chen, S. Kraatz, G.C. Cho, R. Kersting, Identification of a resonant imaging process in apertureless near-field microscopy, Phys. Rev. Lett. 93 (2004) 267401.

[15] N.C.J. van der Valka, P.C.M. Planken, Electro-optic detection of subwavelength terahertz spot sizes in the near field of a metal tip, Appl. Phys. Lett. 81 (2002) 1558–1560.

[16] H.-T. Chen, R. Kerstinga, G.C. Cho, Terahertz imaging with nanometer resolution, Appl. Phys. Lett. 83 (2003) 3009–3011.

[17] P.C.M. Planken, C.E.W.M. van Rijmenam, R.N. Schouten, Opto-electronic pulsed THz systems, Semicond. Sci. Technol. 20 (2005) S121–S127.

[18] S.D. Brorson, R. Buhleier, J.O. White, I.E. Trofimov, H.-U. Habermeier, J. Kuhl, Kinetic inductance and penetration depth of thin superconducting films measured by THz-pulse spectroscopy, Phys. Rev. B 49 (1994) 6185–6187.

[19] D. Grischkowsky, S. Keiding, THz time-domain spectroscopy of high T_c substrates, Appl. Phys. Lett. 57 (1990) 1055–1057.

[20] I. Wilke, M. Khazan, C.T. Rieck, P. Kuzel, T. Kaiser, C. Jaekel, H. Kurz, Terahertz surface resistance of high temperature superconducting thin films, J. Appl. Phys. 87 (2000) 2984–2988.

[21] N. Kida, M. Hangyo, M. Tonouchi, Low-energy charge dynamics in $La_{0.7}Ca_{0.3}MnO_3$: THz time-domain spectroscopic studies, Phys. Rev. B 62 (2000) R11965–R11968.

[22] H. Murakami, T. Kiwa, N. Kida, M. Tonouchi, T. Uchiyama, I. Iguchi, Z. Wang, Partial and macroscopic phase coherences in an underdoped $Bi_2Sr_2CaCu_2O_{8+\delta}$ thin film, Europhys. Lett. 60 (2002) 288–294.

[23] S. Shikii, T. Kondo, M. Yamashita, M. Tonouchi, M. Hangyo, Observation of supercurrent distribution in $YBa_2Cu_3O_7$ thin films using THz radiation excited with femtosecond laser pulses, Appl. Phys. Lett. 74 (1999) 1317–1319.

[24] M. Tonouchi, M. Yamashita, M. Hnagyo, Terahertz radiation imaging of supercurrent distribution in vortex-penetrated $YBa_2Cu_3O_7$ thin film strips, J. Appl. Phys. 87 (2000) 7366–7375.

[25] T. Kiwa, M. Tonouchi, M. Yamashita, K. Kawase, Laser terahertz-emission microscope for inspecting electrical failures in integrated circuits, Opt. Lett. 28 (2003) 2058–2060.

[26] O. Morikawa, M. Yamashita, H. Saijo, M. Morimoto, M. Tonouchi, M. Hangyo, Vector imaging of supercurrent flow in $YBa_2Cu_3O_{7-\delta}$ thin films using terahertz radiation, Appl. Phys. Lett. 75 (1999) 3387–3389.

[27] M. Yamashita, K. Kawase, C. Otani, T. Kiwa, M. Tonouchi, Imaging of large-scale integrated circuits using laser terahertz emission microscopy, Opt. Express 13 (2005) 115–120.

[28] M. Yamashita, K. Kawase, C. Otani, K. Nikawa, M. Tonouchi, Observation of MOSFETs without bias voltage using a laser-THz emission microscope, CLEO2005, 2005, pp. 2117–2119.

[29] M. Yamashita, K. Nikawa, M. Tonouchi, C. Otani, K. Kawase, Backside observation of MOSFET chips using an infrared laser THz emission microscope, in: Proc. The Joint 30th International Conference on Infrared and Millimeter Waves and 13th International Conference on Terahertz Electronics, 2005, pp. 642–643.

[30] K. Takahashi, M. Tonouchi, Influence of Mn doping on ferroelectric-antiferromagnet $BiFeO_3$ thin films grown on $(LaAlO_3)_{0.3}(Sr_2AlTaO_6)_{0.7}$ substrates, Jpn. J. Appl. Phys. 25 (29) (2006) L755–L757.

[31] K. Takahashi, N. Kida, M. Tonouchi, Terahertz radiation by an ultrafast spontaneous polarization modulation of multiferroic $BiFeO_3$ thin films, Phys. Rev. Lett. 96 (2006) 117402–117405.

[32] M. Tonouchi, M. Yamashita, M. Hangyo, Terahertz radiation imaging of supercurrent distribution in vortex-penetrated $YBa_2Cu_3O_{7-\delta}$ thin film strips, J. Appl. Phys. 87 (2000) 7366–7375.

[33] M. Tonouchi, A. Moto, M. Yamashita, M. Hangyo, Terahertz radiation imaging of vortices penetrated into YBCO thin films, IEEE Trans. Appl. Supercond. 11 (1) (March 2001) 3230–3233.

[34] K. Nikawa, S. Inoue, LSI failure analysis using focused laser beam heating, Microelectron. Reliab. 37 (1997) 1841–1847.

[35] K. Nikawa, Laser-SQUID microscope for LSI chip defect analysis, in: T. Kobayashi, H. Hirakawa, M. Tonouchi (Eds.), Vortex Electronics and SQUIDs, Springer, Berlin, 2003, pp. 224–232.

[36] M. Tonocuhi, A. Fujimaki, K. Tanabe, K. Enpuku, K. Nikawa, T. Kobayashi, Recent topics in high-T_c superconductive electronics, Jpn. J. Appl. Phys. 44 (11) (2005) 7735–7749.